J. Phys. Chem. A **2006,** *110,* 7663−7671

Hybrid Density Functional Theory with Specific Reaction Parameter: Hydrogen Abstraction Reaction of Fluoromethane by the Hydroxyl Radical

Titus V. Albu* and Saravanan Swaminathan

Department of Chemistry, Box 5055, Tennessee Technological University, Cookeville, Tennessee 38505

Received: March 13, 2006; In Final Form: April 26, 2006

Three potential energy surfaces with specific reaction parameters are developed and tested for the OH + $CH_3F \rightarrow H_2O + CH_2F$ reaction. The goal of this work is to determine surfaces that provide calculated reaction rate constants that are comparable to the experimental data. The potential energy surfaces are constructed using hybrid and hybrid meta density functional theory methods, and the levels of electronic structure theory used in this study are mPW1PW91, B1B95, and mPW1B95 in conjunction with the 6-31+G(d,p) basis set. The reaction rate constants are calculated over the range 200−1500 K using variational transition state theory with multidimensional tunneling contributions. New specific-reaction-parameter Hartree−Fock contributions are determined, and the hybrid density functional theory methods with these new contributions (35.5 ± 1.2% for mPW1PW91, 36.6 ± 1.2% for B1B95, and 40.7 ± 1.2% for mPW1B95, respectively) reproduce accurate rate constants over an extended temperature range. On these potential energy surfaces, the classical barrier height for the hydrogen abstraction reaction is determined to be 3.4−3.8 kcal/mol, with a best estimate value of 3.6 kcal/mol.

1. Introduction

More than three decades ago, two chemists from the University of California showed that the chlorofluorocarbons (CFCs) could be a major source of inorganic chlorine in the stratosphere, which could become active chlorine (due to their photolytic decomposition by ultraviolet radiation) and destroy the ozone in the stratosphere.[1−4] In 1987, 27 nations signed the “Montreal Protocol to reduce substances that deplete the ozone layer”, an environmental treaty that ensured 50% reduction in the production of CFCs having high ozone depletion potential and global warming potential. The London Amendment to the Protocol in 1990 and the Copenhagen Amendment in 1992 stopped the production of CFC's by January 1, 1996.[3]

Industry developed two classes of halocarbon substitutes—hydrochlorofluorocarbons (HCFCs) and the hydrofluorocarbons (HFCs). However, HCFCs still contain chlorine that makes it possible for them to destroy ozone. The Copenhagen amendment calls for their production to be eliminated by the year 2030.[5] The chlorine-free compounds are considered one of the best substitutes for reducing stratospheric ozone loss. Owing to the zero ozone depletion potential value of HFCs, these compounds have been in focus when they were proposed as replacements to the chlorinated halons. The reactions of fluorinated hydrocarbons with radicals resulting in their decomposition have been in focus due to their role in the nondepletion of the ozone layer. HFCs have a wide range of applications in refrigeration, polyurethane foam production, fire suppressants, rocket fuels, etc. The HFC under consideration in this work is fluoromethane or industrially known as R41. R41 is not only used as a refrigerant but also used as a blowing agent in the polyurethane foam industries. In this work, we consider the attack of a hydroxyl radical on a CH_3F molecule resulting in the abstraction of hydrogen from it to form water. The attack by a hydroxyl radical of the C−H bond in fluoromethane is an important atmospheric reaction due to an increased use of hydrofluorocarbons as substitutes to chlorofluorocarbons. The hydrogen abstraction reaction of fluoromethane by the hydroxyl radical is

$$OH + CH_3F \rightarrow H_2O + CH_2F \tag{1}$$

The kinetics of this reaction has been subject of intense interest and many studies have reported experimentally determined rate constants.[6−12] In some early studies, Howard and Evenson[6] measured the rate constant at 296 K, Nip et al.[7] obtained the rate constant at 297 K, and Jeong and Kaufman[8] measured the rate constants in the temperature range 292−480 K. These experimental results were compiled by Atkinson,[9] and he recommended the following expression for the rate constant between 292 and 480 K:

$$k = 5.51 \times 10^{-18} T^2 \times \exp(-1005 \pm 168/T)\ \mathrm{cm^3\ molecule^{-1}\ s^{-1}} \tag{2}$$

Schmoltner et al.[10] measured the rate constants from 243 to 373 K and fitted the results to the Arrhenius expression:

$$k = 1.75 \times 10^{-12} \exp(-1300/T)\ \mathrm{cm^3\ molecule^{-1}\ s^{-1}} \tag{3}$$

The experimental results showed relatively large uncertainties at the lowest temperatures. Other studies include the one of Hsu and DeMore[11] that studied the reaction from 298 to 363 K and the one of DeMore[12] that used relative rate experiments to measure the rate constants between 308 and 393 K. Combining these data, DeMore[12] fitted the rate constants to an Arrhenius expression:

$$k = 4.4 \times 10^{-12} \exp(-1655/T)\ \mathrm{cm^3\ molecule^{-1}\ s^{-1}} \tag{4}$$

In the present work, the experimentally determined rate constant

---

* Corresponding author. E-mail: albu@tntech.edu.

10.1021/jp0615454 CCC: $33.50

will be considered on the basis of these three rate constant expressions (eqs 2−4).[9,10,12]

There are a large number of theoretical studies focused on this reaction.[13−23] In a recent ab initio and theoretical kinetic study on this reaction, Lien et al.[21] proposed an estimated barrier height of 2.8−3.1 kcal/mol for this reaction based on fitting calculated rate constants to experimental ones. This value is, however, smaller than the calculated values using all ab initio methods investigated in that work or in the work of Korchowiec et al.[18] The rate constant calculations for the title reaction by Lien et al.[21] as well as those of Schwartz et al.[16] and Espinosa-Garcia et al.[17] employed dual-level dynamics calculations that involve corrections to the energy, based on higher-level calculations, along a reaction path determined using a lower level of theory. Dual-level dynamics methods[24−27] are typically used because the dynamics calculations using only the higher level of theory are computationally prohibited and those using only the lower level of theory are commonly inaccurate.

In this study, we use variational transition state theory with multidimensional tunneling contributions (VTST/MT) to calculate the rate constants for the title reaction. We use VTST/MT because it is a powerful and affordable method for studying chemical reaction dynamics. Its accuracy is mainly limited by the level of electronic structure theory used for the potential energy surface (PES) underlying the dynamics. Hybrid density functional theory (HDFT) methods are excellent candidates for generating accurate PES because they are parametrizable and affordable electronic structure methods. Some HDFT methods have been shown to predict accurately a wide variety of molecular and dynamics properties such as molecular geometries, atomization energies, barrier heights, intermolecular interactions, etc.[28−31] We present here a procedure for determining HDFT methods that provide accurate rate constants in conjunction with direct dynamics calculations using VTST/MT. We applied this procedure for developing HDFT methods with a specific reaction parameter (SRP) for the title reaction, and we propose here three new HDFT-SRP methods (with one parameter) that provide accurate rate constants over a wide temperature range. The advantage of the procedure is that we obtain these accurate rate constants for reaction 1 on a single-level potential energy surface rather than using dual-level dynamics techniques. The procedure is applicable to other hydrogen abstraction reactions from HFCs and accurate HDFT methods with SRP (HDFT-SRP) can be generated for different classes of reactions. A similar approach was proposed by Pu and Truhlar for H + CH_4 reactive surface.[32]

The paper is organized as follows: section 2 provides an overview of the theory and computational methodology used, section 3 presents the results, and section 4 gives analyses and discussions. Conclusions and future applications are provided in the final section.

2. Computational Methodology and Quantities Calculated

Variational Transition State Theory with Multidimensional Tunneling Contributions. The rate constants are calculated by using variational transition state theory with multidimensional tunneling contributions (VTST/MT).[33−41] The transition state can be understood classically as a dividing surface (also called generalized transition state) in the phase space that divides the space into a reactant region and a product region.[39,40] In variational transition state theory, the position of the dividing surface is optimized so that the trajectories originated at reactants and passing through the dividing surface in the product region will not recross the surface before being thermalized in the product state. The canonical variational-transition-state theory (CVT) rate constant, k^{CVT}, is obtained by maximizing the generalized free energy of activation (at temperature T), ΔG_T^{GT}, as a function of the position of the generalized transition state along the reaction path. The reaction path is the minimum energy path (MEP) that is defined as the steepest descent path from the saddle point to both the reactant and product sides in the mass weighted (isoinertial) Cartesian coordinate system in which all coordinates are scaled to a common reduced mass μ. The reaction coordinate, s, is defined as the distance along the MEP with the origin located at the saddle point and is positive on the product side and negative on the reactant side. The CVT free energy of activation is obtained as

$$\Delta G_T^{CVT} = \max_s \Delta G_T^{GT}(s) \tag{5}$$

and k^{CVT} is given by

$$k^{CVT}(T) = \sigma \frac{k_B T}{h} \exp(-\Delta G_T^{CVT}/RT) \tag{6}$$

where σ is the symmetry factor accounting for the possibility of more than one symmetry-related reaction path (and can be calculated as the ratio of the product of the reactant rotational symmetry numbers to that of the transition state),[42] k_B is Boltzmann's constant, h is Planck's constant, and R is the gas constant. For this reaction, σ is equal to 3. At the saddle point ($s = 0$) one obtains the conventional TST rate constant, k^{TST}, and the saddle point free energy of activation $\Delta G_T^{\ddagger}$. Any deviation of k^{CVT} from k^{TST} is called a variational effect.

Obtaining k^{CVT} is also equivalent to minimizing the generalized transition state theory rate constants, k^{GT}, with respect to the position s of the generalized transition state along the MEP:

$$k^{CVT}(T) = \min_s \{k^{GT}(T,s)\} \tag{7}$$

where k^{GT} is given by

$$k^{GT}(T,s) = \sigma \frac{k_B T}{h} \frac{Q^{GT}(T,s)}{\Phi^R(T)} \exp(-V_{MEP}(s)/k_B T) \tag{8}$$

In this equation, Q^{GT} is the internal partition function of the generalized transition state with the local zero of energy at $V_{MEP}(s)$ (which is the classical potential energy along the minimum energy path s with its zero of energy at the reactants), and Φ^R is the reactant partition function. Both Q^{GT} and Φ^R are approximated as products of translational, rotational, vibrational, and electronic partition functions. Translational and rotational partition functions were evaluated classically whereas the vibrational partition functions were calculated quantum mechanically within the harmonic approximation for the present study. Although anharmonicity is known to be important,[43,34,44] one can assume a certain amount of cancellation between the anharmonic corrections for the reactant and for the generalized transition states.[34]

Quantum mechanical effects along the reaction coordinate are included in this study in the form of temperature-dependent transmission coefficients, κ. The transmission coefficients primarily account for the multidimensional tunneling. Rate constants including tunneling contributions are computed as

$$k^{CVT/MT}(T) = \kappa^{MT}(T) k^{CVT}(T) \tag{9}$$

where κ^{MT} is the transmission coefficient and is given by

$$\kappa^{MT} = \int_{V_a^R}^{\infty} d(E/RT) P^{MT}(E) \exp\{-[E - V_a^G(s_*^{CVT}(T))]/RT\} \tag{10}$$

where $P^{MT}(E)$ is the ground-state tunneling probability at energy E and $s_*^{CVT}(T)$ is the location of the dynamical bottleneck at T. The tunneling calculation is based in part on $V_a^G(s)$, which is the vibrationally adiabatic ground-state potential energy curve defined, for nonlinear systems, as

$$V_a^G(s) = V_{MEP}(s) + \sum_{m=1}^{3N_{atoms}-7} \frac{\hbar\omega_m(s)}{2} \tag{11}$$

where $\omega_m(s)$ is the frequency of generalized normal mode m at location s along the MEP and N_{atoms} is the total number of atoms in the reactive system (seven for the title reaction). In the present study, the multidimensional transmission coefficients were computed using the centrifugal-dominant, small-curvature, semiclassical, adiabatic, ground-state tunneling (called small-curvature tunneling or SCT) approximation,[45,46] version 4 of the large-curvature tunneling (LCT) approximation,[47−50] and the microcanonical optimized multidimensional tunneling (μOMT) approximation.[47,49] The LCT result includes tunneling into vibrationally excited states. The μOMT result is obtained by selecting, for any total energy, the larger of the SCT and LCT probabilities. We also carry out calculations using the one-dimensional zero-curvature tunneling (ZCT) approximation. In CVT/MT calculations, the tunneling contributions are calculated, for an exothermic reaction, from the ground state of the reactant to the ground and excited states of the product.

Hybrid Density Functional Theory Methods. The electronic structure theory methods for all calculations in this study are HDFT methods. In an HDFT method, the one-parameter hybrid Fock−Kohn−Sham operator can be written as

$$F = F^H + XF^{HFE} + (1 - X)(F^{SE} + F^{GCE}) + F^C \tag{12}$$

where F^H is the Hartree operator (i.e., the nonexchange part of the Hartree−Fock operator), F^{HFE} is the Hartree−Fock exchange operator, X is the fraction of Hartree−Fock (HF) exchange, F^{SE} is the Dirac−Slater local density functional for exchange, F^{GCE} is the gradient correction for the exchange functional, and F^C is the total correlation functional including both local and gradient-corrected parts. The functionals used here are mPW1PW91,[51−53] B1B95,[54−57] and mPW1B95,[52,56,29] in conjunction with the 6-31+G(d,p) basis set. To be exact, whereas mPW1PW91 is a hybrid DFT, mPW1B95 and B1B95 are actually hybrid meta DFT methods but, for simplicity, we will refer in the rest of the paper to all methods as just HDFT methods.

In the specific-reaction-parameter (SRP) approach employed here, we parametrized the value of X in eq 12 to create potential energy surfaces that will generate VTST/MT rate constants nearly identical to the experimental values. We label the hybrid density functional obtained for different values of X by defining the gradient correlated exchanged functional used, followed by 1 to indicate a one-parameter method, followed by the correlation functional used, and finally by the value of X (given as a percent) separated by dash. For example, mPW1PW91-35.7 represents a hybrid density functional theory method based on modified Perdew−Wang (mPW)[52] gradient-corrected exchange functional and PW91[51] gradient-corrected correlation functional with 35.7% HF exchange contribution. The K methods (MPW1K, BB1K, and MPW1K) developed by Truhlar and co-workers[53,57,29] were relabeled according to the convention above as mPW1PW91-42.8, B1B95-42.8, and mPW1B95-44.0, respectively.

TABLE 1: Energetic Parameters for OH + $CH_3F \rightarrow H_2O$ + CH_2F Reaction[a]

HDFT method	ΔE	ΔH	$V^\ddagger$	$\Delta H_0^\ddagger$	$E_a^\ddagger$	$E_a^{V/T}$	$\Delta G_{298}^\ddagger$	$\omega^\ddagger$
mPW1PW91-X/6-31+G(d,p)								
X = 25.0	−14.9	−15.9	0.9	0.0	0.2	n.c.[b]	6.5	494i
X = 33.0	−14.0	−15.0	3.0	1.5	1.7	2.4	8.1	903i
X = 35.7	−13.7	−14.7	3.7	2.1	2.3	2.9	8.7	1042i
X = 42.8	−12.9	−13.9	5.5	3.8	4.0	4.1	10.4	1362i
B1B95-X/6-31+G(d,p)								
X = 28.0	−15.2	−16.3	0.6	−0.1	0.1	n.c.	6.4	385i
X = 34.3	−14.1	−15.1	3.0	1.6	1.8	2.5	8.1	833i
X = 37.0	−13.8	−14.8	3.6	2.1	2.3	3.0	9.3	971i
X = 42.0	−13.2	−14.2	4.9	3.2	3.4	3.8	9.8	1207i
mPW1B95-X/6-31+G(d,p)								
X = 31.0	−14.7	−15.8	1.2	0.0	0.2	n.c.	6.5	620i
X = 38.0	−13.9	−14.9	3.0	1.5	1.7	2.3	8.0	984i
X = 41.0	−13.5	−14.5	3.8	2.2	2.4	2.9	9.4	1131i
X = 44.0	−13.2	−14.2	4.5	2.9	3.1	3.4	9.5	1265i

[a] All values are in kcal/mol except the imaginary frequency that is in cm^{-1}. [b] n.c. denotes not calculated.

Computational Details. All electronic structure calculations are carried out using the *Gaussian* 03 suite of programs.[58] Restricted wave functions are used for closed-shell systems and unrestricted wave functions for open-shell systems. We carry out the geometry optimizations using a tight convergence criteria and an ultrafine integration grid for numerical integrations.

Direct dynamics calculations are carried out with the GAUSSRATE[59] computer program, which interfaces the POLYRATE[60] and GAUSSIAN[58] programs. In calculating the partition function of the hydroxyl radical, we include the $^2\Pi_{1/2}$ electronic excited state with an excitation energy of 140 cm^{-1}. For the generalized transition state, no low-lying electronically excited states are considered so the electronic partition function is the ground-state degeneracy. The MEP in isoinertial coordinates is calculated by the Page−McIver method.[61] In all direct dynamics calculations, the coordinates are scaled to a reduced mass μ of 1 amu. A step size of 0.005 a_0 between gradient calculations is used, and a Hessian is calculated every 0.05 a_0 along the MEP. Calculations are carried out far enough along the reaction path to fully converge the tunneling calculations. The vibrational frequencies along the reaction path are evaluated using a set of redundant internal coordinates[62] that consists of six stretches, eleven nondegenerate bends, and one torsion. These choices of the redundant internal coordinates that are used in generalized, normal-mode, vibrational analyses, yielded in each case a reaction-path Hamiltonian with all frequencies real along MEP in the region relevant to the kinetics. The partition functions are calculated assuming the rigid rotor-harmonic oscillator approximation.

3. Results

The results of our calculations are presented in three tables and seven figures. In Table 1, we present energetic parameters for reaction 1 calculated with different HDFT methods. In this table, ΔE is the classical energy of reaction, ΔH is the zero-point-inclusive energy of reaction, $V^\ddagger$ is the classical (i.e., zero-point-exclusive) barrier height, $\Delta H_0^\ddagger$ is the zero-point-inclusive barrier height, $E_a^\ddagger$ is Arrhenius activation energy at 298 K obtained on the basis of k^{TST}, $E_a^{V/T}$ is Arrhenius activation energy at 298 K obtained on the basis of $k^{CVT/\mu OMT}$, $\Delta G_{298}^\ddagger$ is

TABLE 2: Geometric Parameters for the Saddle Point of $OH + CH_3F \rightarrow H_2O + CH_2F$ Reaction[a]

HDFT method	$r^{\ddagger}_{C\cdots H}$	$r^{\ddagger}_{H\cdots O}$	$r^{\ddagger}_{C\cdots O}$	$\theta^{\ddagger}_{C\cdots H\cdots O}$
mPW1PW91-*X*/6-31+G(d,p)				
$X = 25.0$	1.177	1.394	2.566	172.6
$X = 33.0$	1.195	1.339	2.501	172.4
$X = 35.7$	1.199	1.326	2.519	172.3
$X = 42.8$	1.208	1.299	2.501	172.0
B1B95-*X*/6-31+G(d,p)				
$X = 28.0$	1.172	1.417	2.585	173.3
$X = 34.3$	1.194	1.344	2.533	172.9
$X = 37.0$	1.198	1.331	2.528	172.7
$X = 42.0$	1.205	1.310	2.509	172.4
mPW1B95-*X*/6-31+G(d,p)				
$X = 31.0$	1.184	1.369	2.547	172.1
$X = 38.0$	1.197	1.328	2.519	171.9
$X = 41.0$	1.202	1.315	2.511	171.7
$X = 44.0$	1.206	1.304	2.503	171.6

[a] Distances are in Å; angles are in deg.

the free energy of activation at 298 K, and $\omega^{\ddagger}$ is the imaginary frequency at the saddle point. The zero-point-inclusive barrier height, $\Delta H_0^{\ddagger}$, is calculated as

$$\Delta H_0^{\ddagger} = V^{\ddagger} + \sum_{m=1}^{14} \frac{\hbar\omega_m^{\ddagger}}{2} - \sum_{n=1}^{9} \frac{\hbar\omega_n^{CH_3F}}{2} - \frac{\hbar\omega^{OH}}{2} \qquad (13)$$

where $\omega_m^{\ddagger}$ are the frequency of the normal mode m for the saddle point, $\omega_n^{CH_3F}$ is the frequency of the normal mode n of CH_3F, and ω^{OH} is the hydroxyl normal-mode frequency. The Arrhenius activation energies at 298 K, $E_a^{\ddagger}$ and $E_a^{V/T}$, are obtained by fitting k^{TST} and $k^{CVT/\mu OMT}$ to an Arrhenius expression and are calculated as

$$E_a{}^{\ddagger} = \frac{RT_1T_2}{T_2 - T_1} \ln \frac{k^{TST}(T_2)}{k^{TST}(T_1)} \qquad (14)$$

and

$$E_a^{V/T} = \frac{RT_1T_2}{T_2 - T_1} \ln \frac{k^{CVT/\mu OMT}(T_2)}{k^{CVT/\mu OMT}(T_1)} \qquad (15)$$

where $T_1 = 293$ K and $T_2 = 303$ K. In Table 2, we present selected geometric parameters of the saddle points calculated on different HDFT surfaces.

In Table 3, we present the calculated rate constants as well as experimental ones (where available) in the 200−1500 K temperature range. We present in this table only $k^{CVT/\mu OMT}$; some other calculated rate constants are given as Supporting Information. The accuracy of the calculated rate constants using various density functional methods was monitored by means of two statistical measure of the average deviation.[49] We employed the mean unsigned percentage error (MUPE), defined as

$$\text{MUPE} = \left(\frac{1}{N} \sum_{i=1}^{N} \left| \frac{k_i^{calc} - k_i^{exp}}{k_i^{exp}} \right| \right) \times 100\% \qquad (16)$$

and the logarithmically averaged percentage error (LAPE) defined as

$$\text{LAPE} = (10^{\text{AUPD}} - 1) \times 100\% \qquad (17)$$

$$\text{AUPD} = \frac{1}{N} \sum_{i=1}^{N} \left| \log_{10} \frac{k_i^{calc}}{k_i^{exp}} \right| \qquad (18)$$

where k_i^{calc} represents the calculated rate constant at a certain temperature, k_i^{exp} represents the calculated rate constant at the same temperature, and N is the number of different temperature over which the comparison is made. MUPE is very familiar and used more extensively, but it does not give a balanced representation of the cases in which the calculated rate constants are underestimated that are limited to a percent error of 100%. On the other hand, LAPE treats evenly both underestimates and overestimates of the experimental rate constants. MUPE and LUPE are also given in Table 3.

Figure 1 shows V_{MEP} and V_a^G along the reaction coordinate determined with mPW1PW91-35.7, B1B95-37.0, and mPW1B95-41.0 functionals, respectively, and the 6-31+G(d,p) basis set. In these figures, all reported energies are relative to the zero-point-exclusive energy of the reactants, which is considered the zero of energy. In Figure 2, we give a two-dimensional representation of the MEPs calculated at the same levels of theory as Figure 1. Figures 3−5 show Arrhenius representations of the calculated rate constants obtained using the mPW1PW91,

TABLE 3: Calculated ($k^{CVT/\mu OMT}$) and Experimental Rate Constants (in cm^3 $molecule^{-1}$ s^{-1}) Determined on Various Surfaces as Well as the Average Errors

	mPW1PW91-*X*/6-31+G(d,p)			B1B95-*X*/6-31+G(d,p)			mPW1B95-*X*/6-31+G(d,p)			
temp (K)	$X = 33.0$	$X = 35.7$	$X = 42.8$	$X = 34.3$	$X = 37.0$	$X = 42.0$	$X = 38.0$	$X = 41.0$	$X = 44.0$	exp
200	8.2(−15)[a]	2.1(−15)	7.0(−17)	6.9(−15)	1.8(−15)	1.7(−16)	9.8(−15)	2.2(−15)	5.3(−16)	n.a.[b]
250	2.4(−14)	7.4(−15)	4.2(−16)	2.1(−14)	6.8(−15)	9.3(−16)	2.6(−14)	7.3(−15)	2.2(−15)	9.7(−15)
298	5.0(−14)	1.8(−14)	1.5(−15)	4.6(−14)	1.7(−14)	3.1(−15)	5.4(−14)	1.8(−14)	6.3(−15)	2.0(−14)
300	5.1(−14)	1.9(−14)	1.6(−15)	4.8(−14)	1.8(−14)	3.2(−15)	5.6(−14)	1.8(−14)	6.5(−15)	2.0(−14)
350	9.5(−14)	4.0(−14)	4.3(−15)	9.0(−14)	3.8(−14)	8.3(−15)	1.0(−13)	3.8(−14)	1.5(−14)	4.0(−14)
400	1.6(−13)	7.2(−14)	9.9(−15)	1.5(−13)	7.0(−14)	1.8(−14)	1.6(−13)	6.8(−14)	3.0(−14)	7.1(−14)
450	2.4(−13)	1.2(−13)	2.0(−14)	2.3(−13)	1.2(−13)	3.4(−14)	2.5(−13)	1.1(−13)	5.3(−14)	1.2(−13)
500	3.4(−13)	1.8(−13)	3.5(−14)	3.3(−13)	1.8(−13)	5.8(−14)	3.5(−13)	1.7(−13)	8.6(−14)	n.a.
600	6.2(−13)	3.6(−13)	8.8(−14)	6.1(−13)	3.6(−13)	1.4(−13)	6.3(−13)	3.4(−13)	1.9(−13)	n.a.
700	1.0(−12)	6.3(−13)	1.8(−13)	1.0(−12)	6.3(−13)	2.7(−13)	1.0(−12)	6.0(−13)	3.6(−13)	n.a.
800	1.5(−12)	1.0(−12)	3.3(−13)	1.5(−12)	1.0(−12)	4.8(−13)	1.6(−12)	9.6(−13)	6.1(−13)	n.a.
900	2.2(−12)	1.5(−12)	5.5(−13)	2.2(−12)	1.5(−12)	7.7(−13)	2.2(−12)	1.4(−12)	9.5(−13)	n.a.
1000	3.1(−12)	2.1(−12)	8.6(−13)	3.1(−12)	2.2(−12)	1.2(−12)	3.1(−12)	2.1(−12)	1.4(−12)	n.a.
1200	5.3(−12)	3.9(−12)	1.8(−12)	5.4(−12)	4.0(−12)	2.3(−12)	5.3(−12)	3.8(−12)	2.7(−12)	n.a.
1500	1.0(−11)	8.0(−12)	4.1(−12)	1.1(−11)	8.2(−12)	5.2(−12)	1.0(−11)	7.8(−12)	5.9(−12)	n.a.
MUPE	134	6	90	119	9	80	150	9	64	
LAPE	133	7	950	118	11	438	149	10	185	

[a] 8.2(−15) ≡ 8.2 × 10^{-15}. [b] n.a. denotes not available.

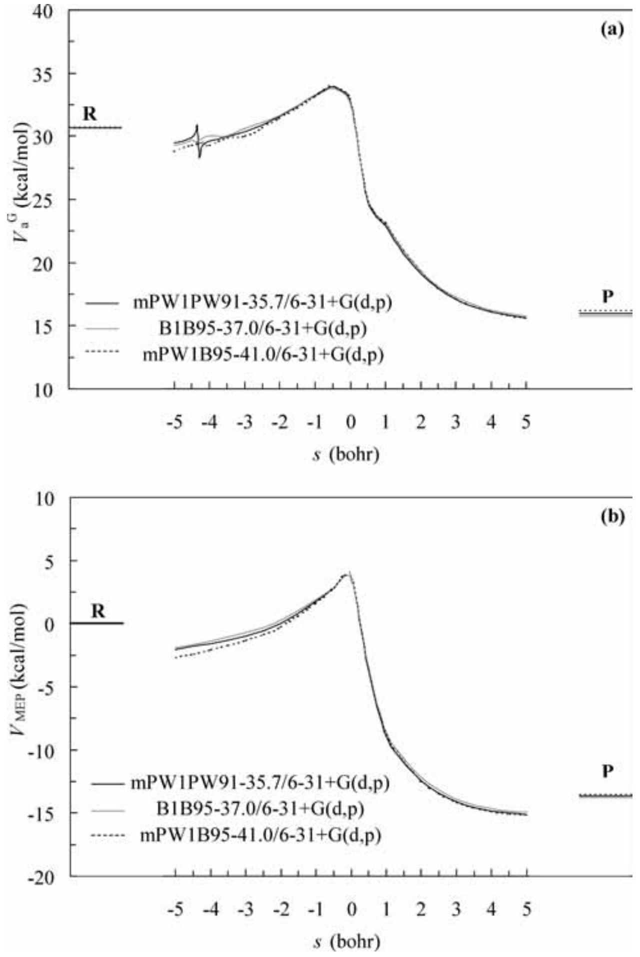

Figure 1. Reaction path profiles ($-5.0\ a_0 < s < +5.0\ a_0$) for OH + $CH_3F \rightarrow H_2O + CH_2F$ reaction determined on the HDFT surfaces that provide accurate calculated rate constants: (a) vibrationally adiabatic ground-state potential energy curves, V_a^G, and (b) potential energy curves along the minimum energy path, V_{MEP}. R represents the reactant state and P represents the product state.

the B1B95, and the mPW1B95 functional, respectively, with different HF contributions. In these three figures, the experimental values obtained from the fit of Atkinson[9] are represented by ∗, the values obtained from the fit of Schmoltner et al.[10] are represented by ×, the values obtained from the fit of DeMore[12] are represented by +, and the experimental values that were used in determining the accuracy of HDFT methods as described below are represented by ○. Figure 6 shows a typical plot of log $k(T)$ versus the HF exchange contribution, in this particular case, showing results obtained using mPW1B95 functional at three different temperatures. Finally, Figure 7 shows LAPE and MUPE in calculated rate constant versus the HF exchange contribution for all three functionals investigated in this study.

4. Analysis and Discussion

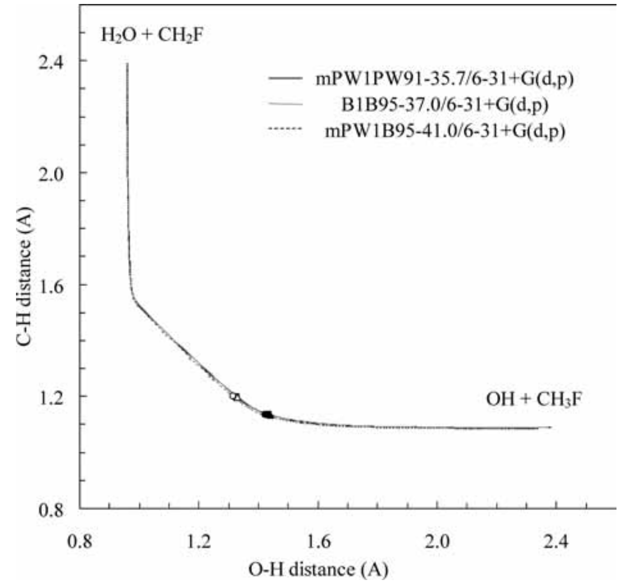

Figure 2. Two-dimensional representation of the reaction paths ($-5.0\ a_0 < s < +5.0\ a_0$) determined using the three HDFT methods that provide accurate calculated rate constants. The open symbols (□ = mPW1PW91, △ = B1B95, ○ = mPW1B95) show the saddle point, $s = 0$; the filled ones show the dynamical bottleneck at 298 K, $s_*^{CVT}(298)$.

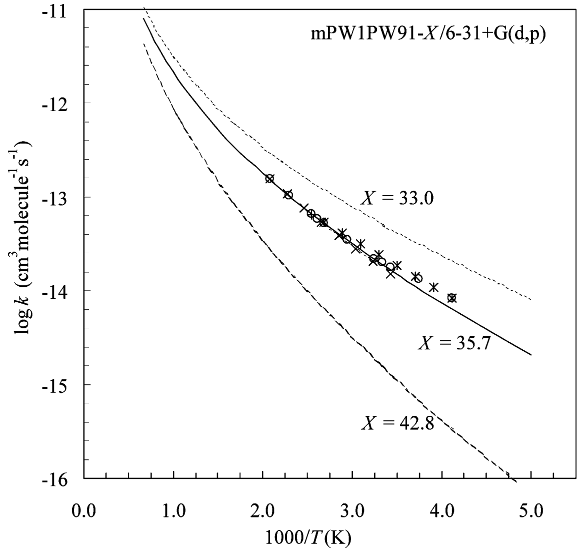

Figure 3. Arrhenius plot of CVT/μOMT rate constants calculated from the three mPW1PW91-X/6-31+G(d,p) surfaces compared with experimental results.

Selection of HDFT Methods. The goal of the study is to determine HDFT methods that provide accurately calculated rate constants using VTST/MT for the title reaction. For each of the three functionals investigated in this study, we initially carried out direct dynamics calculations using PES obtained with functionals designed for kinetics (i.e., the K methods: MPW1K, BB1K, and MPWB1K, respectively). All three functionals provide rate constants that are smaller than the experimental ones due to a high (i.e., overestimated) classical barrier height. We carried out a second set of dynamics calculations using three density functional methods[23] that were determined to have a classical barrier height within the range of best estimate proposed by Lien et al.[21] These three methods are mPW1PW91-33.0, B1B95-34.3, and mPW1B95-38.0, respectively, and all give a classical barrier height of 3.0 kcal/mol (Table 1).[23] The dynamics calculations show that all three methods slightly overestimate the rate constants as a result of a slight underestimate in the classical barrier height (Table 3). On the basis of the results of the two sets of dynamics calculations, assuming a linear relationship between log $k^{CVT/SCT}$ and the HF exchange contribution (X), we determine three new HDFT methods with a SRP value for X that will give calculated rate constant of high accuracy. We choose to determine this SRP value of X by having a target experimental rate constant value (of 3.51×10^{-14} cm^3 molecule^{-1} s^{-1}) at one temperature only (340 K) (the value obtained as an average of the three rate constants (3.31×10^{-14},

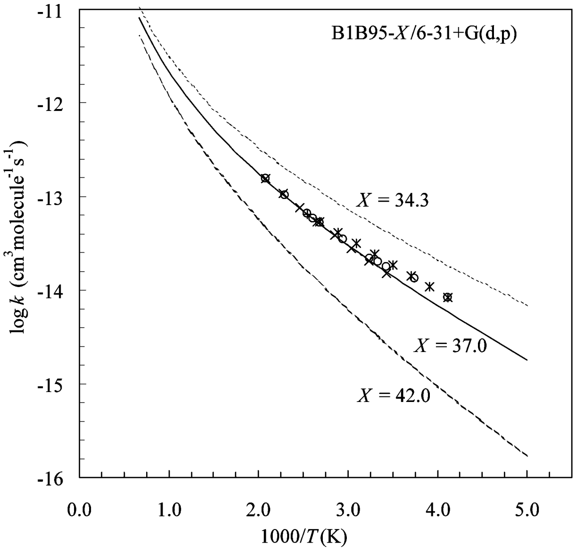

Figure 4. Arrhenius plot of CVT/μOMT rate constants calculated from the three B1B95-*X*/6-31+G(d,p) surfaces compared with experimental results.

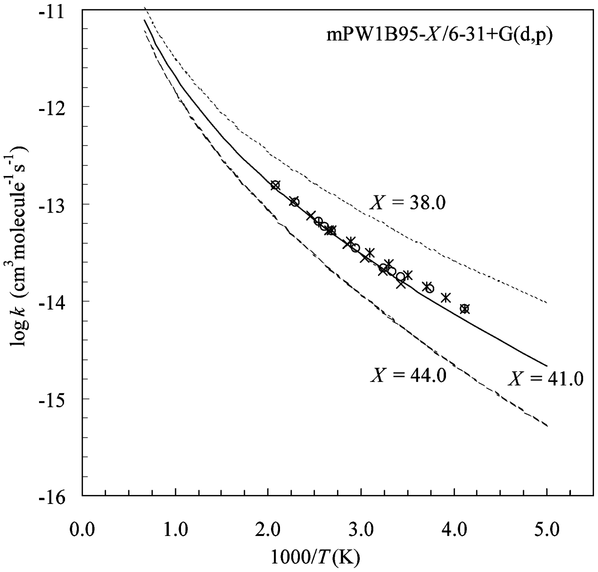

Figure 5. Arrhenius plot of CVT/μOMT rate constants calculated from the three mPW1B95-*X*/6-31+G(d,p) surfaces compared with experimental results.

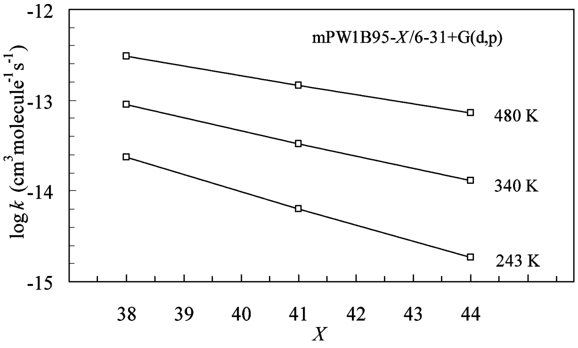

Figure 6. Example of quadratic fits for calculated rate constants at three temperatures (243, 340, and 480 K) determined at the mPW1B95-*X*/6-31+G(d,p) level of theory.

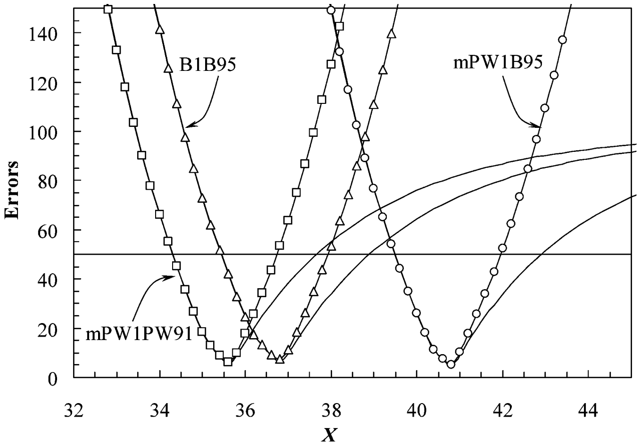

Figure 7. Average percentage error of all three methods as a function of the HF exchange contribution to the exchange-correlation functional. LAPE are the curves with symbols (squares for mPW1PW91-*X*, triangles for B1B95-*X*, and circles for mPW1B95-*X*); MUPE are the curves without symbols.

3.82×10^{-14}, and 3.38×10^{-14} cm^3 molecule^{-1} s^{-1}, respectively) obtained on the basis of the three available experimental fits).[9,10,12] The temperature of 340 K was chosen because this value is the median temperature of the temperature range where all the three fits have been validated. We determined therefore three methods (mPW1PW91-35.7, B1B95-37.0, and mPW1B95-41.0) that, after carrying out dynamics calculations, were established to provide calculated rate constants within acceptable range (10%) of the experimental rate constant at 340 K. In Tables 1 and 2, we present also results obtained for the standard mPW1PW91, B1B95 and mPW1B95 methods ($X = 25.0$, $X = 28.0$, and $X = 31.0$, respectively). These results were determined only from the properties of the saddle point; no dynamics calculations were carried out using these methods.

Calculated Rate Constants and Their Accuracy. The rate constants (including tunneling contributions) calculated on different HDFT surfaces over the temperature range 200−1500 K are given in Table 3. The errors are also given in Table 3, but they are calculated over the smaller temperature range where experimental data are available, as described below. There are three available experimental data fits (given by eqs 2−4) over temperature intervals such that all three of them cover 243−480 K temperature range. The analysis of the accuracy of an HDFT method was carried out using a set of eleven temperatures. These eleven temperatures are the six end points of the three experimental fits (243, 292, 308, 373, 393, and 480 K) and another five temperatures (267, 300, 340, 383, and 436) that are the medians of the five temperature intervals defined by the original six points. On four of these temperatures (the lowest two and the highest two) we have only one experimental fit, and this expression was used to obtain the experimental rate constant at that temperature. For other four temperatures, we have two experimental fits, and the experimental rate constants were obtained as the average of the two values obtained from each available fit. For the middle three temperatures, we have three experimental fits, and the experimental rate constants were obtained as the average of the three values obtained from each available fit.

At each one of these eleven temperatures, we represented log $k^{\mathrm{CVT}/\mu\mathrm{OMT}}$ vs the HF exchange contribution (X), and we fitted this representation to a second-order polynomial that was then used to calculate a rate constant for each value of X within a certain range. (The quadratic polynomial fits are provided as Supporting Information.) A typical representation of the log $k^{\mathrm{CVT}/\mu\mathrm{OMT}}$ vs X dependence is shown in Figure 7. Having log $k^{\mathrm{CVT}/\mu\mathrm{OMT}}$ as a function of the X value, we calculated MUPE and LAPE as a function of the X value. LAPE vs X representations for all three functional examined are given in Figure 7.

This figure shows what is the X value range that one should use to obtain calculated rate constants (using VTST/MT dynamics calculations on a certain PES obtained using HDFT method in conjunction with 6-31+G(d,p) basis set) within a certain desired accuracy with respect to the experimental values. For example, for a 15% average error in the rate constants, one should use quite a narrow range of X: 35.1−35.9 using mPW1PW91, 36.3−37.1 using B1B95, and 40.3−41.1 using mPW1B95 functional, respectively.

In interpreting these results (and in calculating rate constants that are not available experimentally), one should be satisfied (or better said, we would be satisfied) if the error in the calculated rate constants is less than 50%. It is of course preferred to obtained errors much smaller than this, but one should take into account that direct dynamics results using VTST/MT give rate constants that are, on average, within 25−30% of the experimental or the accurate quantum mechanical dynamics rate constants.[49,63,64] Our dynamics calculations also include additional approximations (like not including the anharmonicity or not using scaled vibrational frequencies in calculating vibrational partition functions) that may increase (although they can also decrease) the inaccuracy of the calculated rate constants, so accepting 50% errors in calculated rate constants is reasonable. Our analysis given the ranges of X that provide errors in the calculated rate constants that are within 50% of the experimental data are 34.3−36.7 using mPW1PW91, 35.4−37.9 using B1B95, and 39.5−41.9 using mPW1B95 functional, respectively. The optimal values of X are 35.6 for mPW1PW91, 36.8 for B1B95, and 40.8 for mPW1B95 functional, respectively.

Our direct dynamics shows that the tunneling contributions are not very important for this reaction. At 298 K, the transmission coefficient is the highest for the mPW1B95-41.0 functional ($\kappa^{\mu\text{OMT}} = 1.63$) then the mPW1PW91 functional ($\kappa^{\mu\text{OMT}} = 1.55$) and the smallest for the B1B95-37.0 functional ($\kappa^{\mu\text{OMT}} = 1.38$). The same trend is obtained for the calculated classical barrier height, whereas the imaginary frequency at the saddle point has an opposite behavior.

It is also interesting to point out that among the K methods, mPWB1K give the best results (LAPE = 185) then BB1K (LAPE = 438) then MPW1K (LAPE = 950).

Reaction Energetics. One of the advantages of using HDFT methods in creating PES for dynamics calculations is that the energetics in the saddle point region is very dependent on the HF exchange contribution. Inspecting the results in Table 1, one obvious observation is that the calculated classical barrier height increases with the increase in the HF exchange contribution to the exchange-correlation energy. The generic HDFT methods (with lower values of X) greatly underestimate the barrier height and the HDFT methods designed for kinetics (i.e., the K methods) overestimate the classical barrier height, with calculated values of 5.5, 4.9, and 4.5 kcal/mol for MPW1K, BB1K, and MPWB1K, respectively. The HF exchange contribution that one uses to get a certain barrier height depends on the choice of gradient-corrected exchange and correlation functional used. For example, mPW1PW91-33.0, B1B95-34.3, and mPW1B95-38.0 methods give classical barrier heights of 2.98, 2.96, and 2.99 kcal/mol, respectively (i.e., the same barrier height) by using different HF exchange contributions.

Finally, what is the value of the classical barrier height on HDFT surfaces that give accurate rate constants in conjunction with VTST/MT dynamics calculations? To be more exact, one should find a range of values of X and a range of barrier height values that provide accurate results. For each of these three functionals, we fitted quadratically the three calculated barrier heights vs X and found, on the basis of the fit, and knowing the limits of X that give calculated rate constants within the acceptable accuracy range of 50%, classical barrier heights of 3.31−3.92 kcal/mol for the mPW1PW91 functional, 3.23−3.86 kcal/mol for the B1B95 functional, and 3.38−4.00 kcal/mol for the mPW1B95 functional. Combining the results for all three functionals examined here, we propose a new best estimate range of 3.4−3.8 kcal/mol for the title reaction. (The most accurate rate constants are obtained for surfaces with an average classical barrier height of 3.65 kcal/mol.) This barrier height estimate is higher that that of Lien et al.[21] but is closer to the values calculated with ab initio methods.[18]

The calculated reaction exothermicity is slightly underestimated on all HDFT surfaces when compared to the experimental value of −18.0 kcal/mol at 0 K. The discrepancy increases as the HF exchange contribution increases.

Properties of the Saddle Point and the Dynamical Bottleneck. The results in Table 2 show that the HDFT methods with smaller X values give early transition states characterized by relatively short C···H distances and relatively long H···O distances, whereas HDFT methods with bigger X values give late (or later) transition states. We also investigated the sum of the making ($r^{\ddagger}_{\text{H}\cdots\text{O}}$) and breaking ($r^{\ddagger}_{\text{C}\cdots\text{H}}$) bond distances. This sum, called perpendicular looseness, is a measure of the looseness of the structure in a direction perpendicular to the reaction coordinate. We found that the transition state gets looser as the HF exchange contribution decreases. When only the three methods that give accurate calculates rate constants are compared, the mPW1B95-38.0 method also gives a tighter transition state ($r^{\ddagger}_{\text{C}\cdots\text{H}} + r^{\ddagger}_{\text{H}\cdots\text{O}} = 2.517$ A) whereas the B1B95-34.3 method gives a looser transition state ($r^{\ddagger}_{\text{C}\cdots\text{H}} + r^{\ddagger}_{\text{H}\cdots\text{O}} = 2.529$ A). This difference is mainly due to a longer H···O distance at the transition state. Note also that the C···H···O angle is less than 180° so $r^{\ddagger}_{\text{C}\cdots\text{O}} < r^{\ddagger}_{\text{C}\cdots\text{H}} + r^{\ddagger}_{\text{H}\cdots\text{O}}$. For the HDFT methods used in this study and the 6-31+G(d,p) basis set, the C···H···O angle is around 172°. The reactions paths as well as the saddle point location are represented in Figure 2.

The imaginary frequency at the saddle point can be seen as a measure of the thickness of the barrier. A high imaginary frequency indicates a large negative force constant for the reaction coordinate mode at the saddle point and therefore a thin barrier. A thin barrier results in systematic overestimates of the tunneling probability in dynamics calculations. The mPW1B95 functional gives the narrowest barrier (highest value for the imaginary frequency) and the B1B95 functional gives the widest barrier. The transmission coefficient follows an opposite trend. Based on our results, the best estimate of the imaginary frequency at the saddle point is between 950i and 1150i cm^{-1}. For the three new HDFT methods that give classical barrier heights of same value (mPW1PW91-33.0, B1B95-34.3, and mPW1B95-38.0), the imaginary frequency at the saddle point correlates with the energy difference between the saddle point and the van der Waals complexes that reactants ($CH_3F\cdots OH$) and products ($CH_2F\cdots H_2O$) form.[23]

The dynamical bottleneck at 298 K is located at $s = -0.309$ a_0, $s = -0.320$ a_0, and $s = 0.287$ a_0 using the mPW1PW91-35.7, B1B95-37.0, and mPW1B95-41.0 methods, respectively. These results show quite large variational effects for this reaction, which result also in significant differences between calculated k^{CVT} and k^{TST} (see the rate constants given as Supporting Information). At the dynamical bottleneck, the C···H distance is determined to be 1.134−1.135 Å with all three HDFT methods above and the O···H distance is determined to be between 1.423 Å (using the mPW1B95-41.0 method) and 1.440 Å (using the B1B95-37.0 method).

Further Analysis and Discussion. HDFT methods tend to overestimate the calculated vibrational frequencies. The usual solution is to adjust the calculated values by multiplying the frequency with a scaling factor. For HDFT methods, the scaling factors have values that are smaller than one. A smaller than one scaling factor will reduce the value of the calculated vibrational frequencies leading to larger vibrational partition functions. This is more significant for low-frequency modes so it is expected that, in VTST/MT calculations, the vibrational partition function for generalized transition state will be increased more than that of the reactant, increasing therefore the calculated rate constant. On three HDFT surfaces (given by the K methods), we carried out additional dynamics calculations in which we scaled the calculated frequencies using scaling factors that are available in the literature. For the mPW1PW91-42.8/6-31+G(d,p) surface, we used a scaling factor of 0.9515,[65] for the B1B95-42.0/6-31+G(d,p) surface we used a scaling factor of 0.9561,[57] and for the mPW1B95-44.0/6-31+G(d,p) surface we used a scaling factor of 0.9537.[29] We made the comparison for $k^{\mathrm{CVT/SCT}}$ between the dynamics calculations with frequencies scaled and without. We indeed determined that, by scaling the vibrational frequencies, the calculated rate constants increase by 10−15% in the temperature range where experimental data are available (243−480 K). Most of the differences are a result of an increased k^{CVT} (about 10%) but the SCT contribution also increases (less than 5%). Those differences are, however, well within our confidence range of 50%. The rate constants obtained for the scaled-frequency calculations are presented as Supporting Information. Similar to scaling frequencies with a scaling factor smaller than unity, the inclusion of anharmonicity effects should result in increasing the calculated rate constants. We are, however, expecting that the rate constant deviations will also fall within our confidence range.

We determined how much our results (the X value in our SRP methods and the best estimate of the classical barrier height) would change if, by improving the dynamics theory used, the calculated rate constants change by 15%. For all three functional investigated here, we determined that a decrease of optimal X value by 0.4 (that is equivalent to a smaller classical barrier height by 0.10 kcal/mol) produces rate constants that are 15% larger than the values reported here. Similar results are obtained for rate constants that are 15% smaller.

Inspecting the results in the Supporting Information, one can observe that the title reaction is dominated by small-curvature tunneling. Specifically, the small-curvature tunneling rate constants, $k^{\mathrm{CVT/SCT}}$, are almost always larger than the large-curvature tunneling rate constants, $k^{\mathrm{CVT/LCT}}$. The only exceptions are the rate constants obtained from the mPW1PW91-33.0 surface, for which $k^{\mathrm{CVT/LCT}}$ is larger (but never more than 2% bigger) than $k^{\mathrm{CVT/SCT}}$ at certain temperatures. As a result, the microcanonical optimized multidimensional-tunneling rate constants, $k^{\mathrm{CVT/\mu OMT}}$, are almost always equal to the small-curvature tunneling rate constants. In cases such as this, because the calculation of $k^{\mathrm{CVT/\mu OMT}}$ is more demanding than that of $k^{\mathrm{CVT/SCT}}$, it is preferred to calculate only $k^{\mathrm{CVT/SCT}}$. We actually carried out a full analysis based on $k^{\mathrm{CVT/SCT}}$ (instead of $k^{\mathrm{CVT/\mu OMT}}$) and we found essentially the same results. The only significant difference is in the optimal X value for mPW1PW91 functional, which is, when calculated on the basis of $k^{\mathrm{CVT/SCT}}$, smaller by just 0.1 than when calculated on the basis of $k^{\mathrm{CVT/\mu OMT}}$. Although more studies are necessary to support the assumption, one can presume that other hydrogen abstraction reactions from hydrofluorocarbons by hydroxyl radical are dominated by small-curvature tunneling as well and can calculate dynamics quantities based on more affordable SCT approximation only.

5. Summary and Concluding Remarks

HDFT methods are quite flexible in the choice of exchange and correlation functional that one uses, and this property makes them very attractive methods for use in reaction dynamics studies. Our interest is in obtaining HDFT methods that can be used for accurately investigating chemical dynamics of important environmental and atmospheric processes.

In this work, we have developed three potential energy surfaces with specific reaction parameters for the reaction OH + $CH_3F \rightarrow H_2O + CH_2F$ based on hybrid density functional theory methods. These new methods, in conjunction with the 6-31+G(d,p) basis set, can be used in calculating dynamic properties on an accurate PES surface without the use of dual-level dynamics. All three SPR surfaces have a classical barrier height around 3.6 kcal/mol, which is our best estimate for this reaction.

We carried out direct dynamics calculations on these surfaces using canonical variational transition state theory with microcanonical optimized multidimensional tunneling approximation between 200 and 1500 K. The dynamics results on these surfaces are in excellent agreement with available experimental data over a large temperature range. Using similar methodology, we are currently investigating the hydrogen abstraction reactions from the other fluoromethanes[66] as well as fluoroethanes[67] to determine if the methods developed here are as accurate for these processes as they are for the title reaction. This specific-reaction-parameter methodology is also promising for direct dynamics studies of hydrogen abstraction reactions from more complex hydrofluorocarbons as well as other fluorinated compounds.

The keywords to carry out mPW1PW91-35.7 calculations in Gaussian03 are mPWPW91/6-31+G(d,p) and IOp(3/76=0643003570). The keywords to carry out B1B95-37.0 calculations in Gaussian 03 are BB95/6-31+G(d,p) and IOp(3/76=0630003700). The keywords to carry out mPW1B95-41.0 calculations in Gaussian 03 are mPWB95/6-31+G(d,p) and IOp-(3/76=0590004100).

Acknowledgment. This research was supported in part by Oak Ridge Associated Universities through a Ralph Powe Junior Faculty Enhancement Award and by Tennessee Technological University through a Faculty Research Initiation Program.

Supporting Information Available: Rate constants calculated various direct dynamics methods, the optimized structures, energies and frequencies for the reactants, the products and the saddle points, the parameters for log $k^{\mathrm{CVT/\mu OMT}}$ vs X quadratic fits. This material is available free of charge via the Internet at http://pubs.acs.org.

References and Notes

(1) Molina, M. J.; Rowland, F. S. *Nature* **1974**, *249*, 810.
(2) Molina, M. J.; Rowland, F. S. *J. Phys. Chem.* **1975**, *79*, 667.
(3) Elkins, J. W. In *Encyclopedia of Environmental Science*; Alexander, D. E., Fairbridge, R. W., Eds.; Kluwer Academic: Boston, MA, 1999; p 78.
(4) Brasseur, G. P.; Orlando, J. J.; Tyndall, G. S. *Atmospheric Chemistry and Global Change*; Oxford University Press: New York, 1999.
(5) Creazzo J. A.; Hammel H. S.; Cicalo K. J.; P., S. Zero-ODP Blowing Agents for Polyurethane Foams. Polyurethane World Congress, 1993.
(6) Howard, C. J.; Evenson, K. M. *J. Chem. Phys.* **1976**, *64*, 197.

(7) Nip, W. S.; Singleton, D. L.; Overend, R.; Paraskevopoulos, G. *J. Phys. Chem.* **1979**, *83*, 2440.

(8) Jeong, K. M.; Kaufman, F. *J. Phys. Chem.* **1982**, *86*, 1808.

(9) Atkinson, R. *Chem. Rev.* **1986**, *86*, 69.

(10) Schmoltner, A. M.; Talukdar, R. K.; Warren, R. F.; Mellouki, A.; Goldfarb, L.; Gierczak, T.; McKeen, S. A.; Ravishankara, A. R. *J. Phys. Chem.* **1993**, *97*, 8976.

(11) Hsu, K. J.; DeMore, W. B. *J. Phys. Chem.* **1995**, *99*, 1235.

(12) DeMore, W. B. *J. Phys. Chem.* **1996**, *100*, 5813.

(13) Cohen, N.; Benson, S. W. *J. Phys. Chem.* **1987**, *91*, 162.

(14) Jeong, K. M.; Kaufman, F. *J. Phys. Chem.* **1982**, *86*, 1816.

(15) Bottoni, A.; Poggi, G.; Emmi, S. S. *THEOCHEM* **1993**, *98*, 299.

(16) Schwartz, M.; Marshall, P.; Berry, R. J.; Ehlers, C. J.; Petersson, G. A. *J. Phys. Chem. A* **1998**, *102*, 10074.

(17) Espinosa-Garcia, J.; Coitino, E. L.; Gonzalez-Lafont, A.; Lluch, J. M. *J. Phys. Chem. A* **1998**, *102*, 10715.

(18) Korchowiec, J.; Kawahara, S.-I.; Matsumura, K.; Uchimaru, T.; Sugie, M. *J. Phys. Chem. A* **1999**, *103*, 3548.

(19) Louis, F.; Gonzalez, C. A.; Huie, R. E.; Kurylo, M. J. *J. Phys. Chem. A* **2000**, *104*, 8773.

(20) El-Taher, S. *Int. J. Quantum Chem.* **2001**, *84*, 426.

(21) Lien, P.-Y.; You, R.-M.; Hu, W.-P. *J. Phys. Chem. A* **2001**, *105*, 2391.

(22) Korchowiec, J. *J. Phys. Org. Chem.* **2002**, *15*, 524.

(23) Mikel, S. E.; Albu, T. V. *J. Und. Chem. Res.* **2006**, *5*, 75.

(24) Hu, W. P.; Liu, Y. P.; Truhlar, D. G. *J. Chem. Soc., Faraday Trans.* **1994**, *90*, 1715.

(25) Corchado, J. C.; Coitino, E. L.; Chuang, Y.-Y.; Fast, P. L.; Truhlar, D. G. *J. Phys. Chem. A* **1998**, *102*, 2424.

(26) Chuang, Y.-Y.; Corchado, J. C.; Truhlar, D. G. *J. Phys. Chem. A* **1999**, *103*, 1140.

(27) Albu, T. V.; Corchado, J. C.; Truhlar, D. G. *J. Phys. Chem. A* **2001**, *105*, 8465.

(28) Coote, M. L. *J. Phys. Chem. A* **2004**, *108*, 3865.

(29) Zhao, Y.; Truhlar, D. G. *J. Phys. Chem. A* **2004**, *108*, 6908.

(30) Andersson, S.; Gruening, M. *J. Phys. Chem. A* **2004**, *108*, 7621.

(31) Zhao, Y.; Truhlar, D. G. *J. Phys. Chem. A* **2005**, *109*, 5656.

(32) Pu, J.; Truhlar, D. G. *J. Chem. Phys.* **2002**, *116*, 1468.

(33) Garrett, B. C.; Truhlar, D. G. *J. Chem. Phys.* **1979**, *70*, 1593.

(34) Garrett, B. C.; Truhlar, D. G. *J. Chem. Phys.* **1984**, *81*, 309.

(35) Truhlar, D. G.; Garrett, B. C. *Annu. Rev. Phys. Chem.* **1984**, *35*, 159.

(36) Truhlar, D. G.; Garrett, B. C.; Hipes, P. G.; Kuppermann, A. *J. Chem. Phys.* **1984**, *81*, 3542.

(37) Truhlar, D. G.; Isaacson, A. D.; Garrett, B. C. In *Theory of Chemical Reaction Dynamics*; Baer, M., Ed.; CRC Press: Boca Raton, FL, 1985; Vol. 4; p 65.

(38) Kreevoy, M. M.; Truhlar, D. G. In *Investigation of Rates and Mechanisms of Reactions*; Bernasconi, C. F., Ed.; John Wiley & Sons: New York, 1986; Vol. 6, p 13.

(39) Tucker, S. C.; Truhlar, D. G. In *New Theoretical Concepts Understanding Organic Reactions*; J. Bertran, I. G. C., Ed.; Kluwer Academic Publishers: Dordrecht, The Netherlands, 1989; Vol. 267, p 291.

(40) Truhlar, D. G.; Garrett, B. C.; Klippenstein, S. J. *J. Phys. Chem.* **1996**, *100*, 12771.

(41) Garrett, B. C.; Truhlar, D. G. In *Theory and Applications of Computational Chemistry: The First Forty Years*; Dykstra, C. E., Frenking, G., Kim, K., Scuseria, G., Eds.; Elsevier: Amsterdam, 2005; p 67.

(42) Bell, R. L.; Truong, T. N. *J. Chem. Phys.* **1994**, *101*, 10442.

(43) Garrett, B. C.; Truhlar, D. G. *J. Phys. Chem.* **1979**, *83*, 1915.

(44) Lin, H.; Zhao, Y.; Ellingson, B. A.; Pu, J.; Truhlar, D. G. *J. Am. Chem. Soc.* **2005**, *127*, 2830.

(45) Lu, D.-H.; Truong, T. N.; Melissas, V. S.; Lynch, G. C.; Liu, Y.-P.; Garrett, B. C.; Steckler, R.; Isaacson, A. D.; Rai, S. N.; Hancock, G. C.; Lauderdale, J. G.; Joseph, T.; Truhlar, D. G. *Comput. Phys. Commun.* **1992**, *71*, 235.

(46) Liu, Y. P.; Lynch, G. C.; Truong, T. N.; Lu, D. H.; Truhlar, D. G.; Garrett, B. C. *J. Am. Chem. Soc.* **1993**, *115*, 2408.

(47) Liu, Y. P.; Lu, D. H.; Gonzalez-Lafont, A.; Truhlar, D. G.; Garrett, B. C. *J. Am. Chem. Soc.* **1993**, *115*, 7806.

(48) Truong, T. N.; Lu, D.-H.; Lynch, G. C.; Liu, Y.-P.; Melissas, V. S.; Steward, J. J. P.; Steckler, R.; Garrett, B. C.; Isaacson, A. D.; Gonzalez-Lafont, A.; Rai, S. N.; Hancock, G. C.; Joseph, T.; Truhlar, D. G. *Comput. Phys. Commun.* **1993**, *75*, 143.

(49) Allison, T. C.; Truhlar, D. G. In *Modern Methods for Multidimensional Dynamics Computations in Chemistry*; Thompson, D. L., Ed.; World Scientific: Singapore, 1998; p 618.

(50) Fernandez-Ramos, A.; Truhlar, D. G. *J. Chem. Phys.* **2001**, *114*, 1491.

(51) Perdew, J. P.; Chevary, J. A.; Vosko, S. H.; Jackson, K. A.; Pederson, M. R.; Singh, D. J.; Fiolhais, C. *Phys. Rev. B* **1992**, *46*, 6671.

(52) Adamo, C.; Barone, V. *J. Chem. Phys.* **1998**, *108*, 664.

(53) Lynch, B. J.; Fast, P. L.; Harris, M.; Truhlar, D. G. *J. Phys. Chem. A* **2000**, *104*, 4811.

(54) Becke, A. D. *Phys. Rev. A* **1988**, *38*, 3098.

(55) Becke, A. D. *J. Chem. Phys.* **1993**, *98*, 5648.

(56) Becke, A. D. *J. Chem. Phys.* **1996**, *104*, 1040.

(57) Zhao, Y.; Lynch, B. J.; Truhlar, D. G. *J. Phys. Chem. A* **2004**, *108*, 2715.

(58) Frisch, M. J.; Trucks, G. W.; Schlegel, H. B.; Scuseria, G. E.; Robb, M. A.; Cheeseman, J. R.; Montgomery, J. A., Jr.; Vreven, T.; Kudin, K. N.; Burant, J. C.; Millam, J. M.; Iyengar, S. S.; Tomasi, J.; Barone, V.; Mennucci, B.; Cossi, M.; Scalmani, G.; Rega, N.; Petersson, G. A.; Nakatsuji, H.; Hada, M.; Ehara, M.; Toyota, K.; Fukuda, R.; Hasegawa, J.; Ishida, M.; Nakajima, T.; Honda, Y.; Kitao, O.; Nakai, H.; Klene, M.; Li, X.; Knox, J. E.; Hratchian, H. P.; Cross, J. B.; Adamo, C.; Jaramillo, J.; Gomperts, R.; Stratmann, R. E.; Yazyev, O.; Austin, A. J.; Cammi, R.; Pomelli, C.; Ochterski, J. W.; Ayala, P. Y.; Morokuma, K.; Voth, G. A.; Salvador, P.; Dannenberg, J. J.; Zakrzewski, V. G.; Dapprich, S.; Daniels, A. D.; Strain, M. C.; Farkas, O.; Malick, D. K.; Rabuck, A. D.; Raghavachari, K.; Foresman, J. B.; Ortiz, J. V.; Cui, Q.; Baboul, A. G.; Clifford, S.; Cioslowski, J.; Stefanov, B. B.; Liu, G.; Liashenko, A.; Piskorz, P.; Komaromi, I.; Martin, R. L.; Fox, D. J.; Keith, T.; Al-Laham, M. A.; Peng, C. Y.; Nanayakkara, A.; Challacombe, M.; Gill, P. M. W.; Johnson, B.; Chen, W.; Wong, M. W.; Gonzalez, C.; Pople, J. A. *Gaussian 03*, revision B.02; Gaussian, Inc.: Pittsburgh, PA, 2003.

(59) Corchado, J. C.; Chuang, Y.-Y.; Coitiño, E. L.; Truhlar, D. G. GAUSSRATE 9.1; University of Minnesota: Minneapolis, MN, 2003.

(60) Corchado, J. C.; Chuang, Y.-Y.; Fast, P. L.; Villà, J.; Hu, W.-P.; Liu, Y.-P.; Lynch, G. C.; Nguyen, K. A.; Jackels, C. F.; Melissas, V. S.; Lynch, B. J.; Rossi, I.; Coitiño, E. L.; Fernandez-Ramos, A.; Pu, J.; Albu, T. V.; Steckler, R.; Garrett, B. C.; Isaacson, A. D.; Truhlar, D. G. POLYRATE 9.1; University of Minnesota: Minneapolis, MN, 2003.

(61) Page, M.; McIver, J. W., Jr. *J. Chem. Phys.* **1988**, *88*, 922.

(62) Chuang, Y.-Y.; Truhlar, D. G. *J. Phys. Chem. A* **1998**, *102*, 242.

(63) Pu, J.; Corchado, J. C.; Truhlar, D. G. *J. Chem. Phys.* **2001**, *115*, 6266.

(64) Pu, J.; Truhlar, D. G. *J. Chem. Phys.* **2002**, *117*, 1479.

(65) Lynch, B. J.; Truhlar, D. G. *J. Phys. Chem. A* **2001**, *105*, 2936.

(66) Albu, T. V.; Swaminathan, S. Manuscript in preparation.

(67) Albu, T. V.; De Silva, N. W. S. V. N. Work in progress.